Available online at www.sciencedirect.com
ScienceDirect
Trans. Nonferrous Met. Soc. China 33(2023) 1701−1714
Transactions of Nonferrous Metals Society of China
www.tnmsc.cn

Evolution of precipitate orientation and its effect on thermal conductivity of Mg−5Sn alloy

Li-ping ZHONG, Yong-jian WANG

Institute of Microstructure and Micro/nano-mechanics, School of Metallurgical Engineering, Anhui University of Technology, Maanshan 243002, China

Received 27 December 2021; accepted 20 April 2022

Abstract: The evolution of precipitate orientation and its effect on the thermal conductivity of Mg−5Sn alloys under different treatments were systematically investigated. The results show that for the alloy subjected to aging prior to twinning (Sample AT), the basal precipitates are precisely regulated to be the prismatic precipitates, and the lath-shaped precipitates experience a rigid rotation of 3.7° to accommodate the twinning shear. For hexagon-shaped precipitates with a larger thickness in Sample AT, the precipitate only experiences a small rigid rotation of 0.2°, due to the development of stacking faults releasing part of the strain at the precipitate/twin interface. In addition, the orientation of precipitates has a significant effect on the thermal conductivity of the alloy. When the measurement direction of thermal conductivity is parallel to extrusion direction (ED), the precipitates lying on the basal plane, perpendicular to ED, are more beneficial to the improvement of thermal conductivity than precipitates lying on the prismatic plane parallel to ED. Sample TA (aging after twinning) with precipitates lying on the basal plane shows the best thermal conductivity of 137.81 W/(m·K).

Key words: precipitate; orientation relationship; thermal conductivity; Mg−Sn alloy

1 Introduction

Modern magnesium (Mg) alloys, especially those free of rare earth (RE) elements, such as Mg−Al and Mg−Sn alloys, suffer poor absolute strengths [1]. It has been a limitation that cannot be ignored for wide industrial applications. In addition, thermal conductivity, as one of the most important physical properties, is essential in selecting materials for certain applications [2,3]. And pure Mg shows the best thermal conductivity of 158 W/(m·K) among various metallic Mg alloys and may potentially help meet the increasing demand for heat dispersing materials in modern industry. However, according to the present reports, achieving good mechanical properties and receivable thermal performance appears to be contradictory [4]. Enhancing the strength of materials without sacrificing thermal conductivity remains an important focus in material research.

Precipitation is one of the most effective methods to simultaneously improve the mechanical properties and thermal conductivity of Mg alloys [5,6]. For the strength of alloys, precipitation strengthening is usually enhanced by increasing the volume fraction and decreasing the size of precipitates, as well reported in Mg−Al, Mg−Sn and Mg−Zn alloys [7,8]. In addition, according to the Orowan rule, the orientation of precipitates has a significant effect on the mechanical properties, which has been widely studied [9,10]. While, the research on the effects of precipitation on thermal conductivity of Mg alloys mainly focuses on the influence of the number density of precipitates and the interface between precipitates and matrix [5,6]. But, how the precipitate orientation influences the thermal conductivity of Mg alloys has not been

Corresponding author: Yong-jian WANG, Tel: +86-19155520135, E-mail: wyjcqu@163.com
DOI: 10.1016/S1003-6326(23)66215-6

discussed intently. According to recent studies, the orientation of precipitates can be regulated by coupling twinning, aging and de-twinning in Mg−Al and Mg−Sn alloys [9−11]. Therefore, to obtain different precipitate orientations in Mg alloy, Mg−Sn alloy was selected for investigation by coupling aging and twinning treatments in this study.

Another issue worthy of attention is the interactions of precipitates and $\{10\bar{1}2\}$ tension twin during twinning. As reported in recent works, these lath-shaped particles in Mg−Al and Mg−Sn alloys can be sheared in the twin with a rigid rotation of 3.7° [9,10]. However, according to previous reports, twins can act with precipitates in three different behaviors. And the type of behavior strongly depends on the particle characteristics, such as the particle's thickness and shape [12−14]. For Mg−Sn alloy, the alloy contains several types of precipitates, the interactions between precipitates and $\{10\bar{1}2\}$ tension twin may exhibit different behaviors.

Therefore, in this work, the orientation relationship (OR) between precipitates and α-Mg matrix and the interactions of precipitate and $\{10\bar{1}2\}$ tension twin were systematically analyzed based on the transmission electron microscopy (TEM) in as-extruded Mg−5Sn alloy. And the effect of precipitate orientation on the thermal conductivity of Mg−5Sn alloys was discussed intently.

2 Experimental

Mg−5Sn (wt.%) alloy with a diameter of 85 mm was prepared by a semi-continuous casting. The chemical composition of as-cast alloy was measured by an XRF−1800CCDE X-ray fluorescence spectrometer and the corresponding results are given in Table 1. The as-cast billet was solution-treated at 480 ℃ for 16 h and then quenched into water of 70 ℃. Then, the solution-treated alloy was extruded at 320 ℃ with an extrusion speed of 8 mm/s and an extrusion ratio of 28:1. The as-extruded rods were subjected to an annealing treatment at 400 ℃ for 1 h to obtain a relatively homogeneous microstructure. The cylinder specimens with a diameter of 12 mm and a height of 20 mm were cut from the as-annealed rods along the extrusion direction (ED). The specimen subjected to aging after twinning was denoted as Sample TA, the specimen subjected to aging prior to twinning was denoted as Sample AT, and the specimen subjected to aging was denoted as Sample A. In addition, aging treatment was carried out at 200 ℃ for 500 h. Due to low precipitation kinetic of Mg−Sn alloy and in order to reduce the content of solute atoms in the matrix, the aging time of 500 h was chosen. Then, the samples were compressed to a strain of 8%. The compressive tests were carried out on an MTS precision universal tester (CMT5105) at room temperature with a strain rate of 1×10^{-3} s^{-1}. The schematic diagrams of Samples TA and AT processes are illustrated in Fig. 1.

Table 1 Actual composition of as-cast Mg−5Sn alloy (wt.%)

Mn	Al	Zn	Sn	Mg
0.008	0.004	0.002	5.15	Bal.

Microstructure observations and texture analysis of all samples were examined by electron backscattered diffraction analysis (EBSD, FEI Scios) equipped with an HKL Symmetry EBSD detector. EBSD preparation consisted of mechanical grinding on SiC papers with grit sizes of 400#, 600#, 800#, 1000# and 1200#, washing, blow-drying as well as Ar ion polishing for approximately 70 min. The step size of EBSD analysis for Sample A was set as 2 μm, while for Samples TA and AT, the step size was set as 0.5 μm. All EBSD data were analyzed by Channel 5 software. The precipitation behavior and ORs between precipitates and matrix were characterized by transmission electron microscopy (TEM, Tecnai G2 F20 S-TWIN), high resolution TEM (HRTEM) and selected area electron diffraction (SAED) operated at 200 kV. Thin foils for TEM observation were prepared by mechanical polishing to ~50 μm, and then ion beam thinning by GATAN, PIPS 691 device. In addition, diffraction patterns were simulated by PTCLab software [15].

Specimens for thermal diffusivity measurements were cut from samples perpendicular to ED in the shape of disks with dimensions of d12.5 mm × 2.5 mm, which were carried out on a Netzsch 457 apparatus via laser flash method at 303 K. The measurement direction of thermal diffusivity was parallel to ED. The room temperature density was

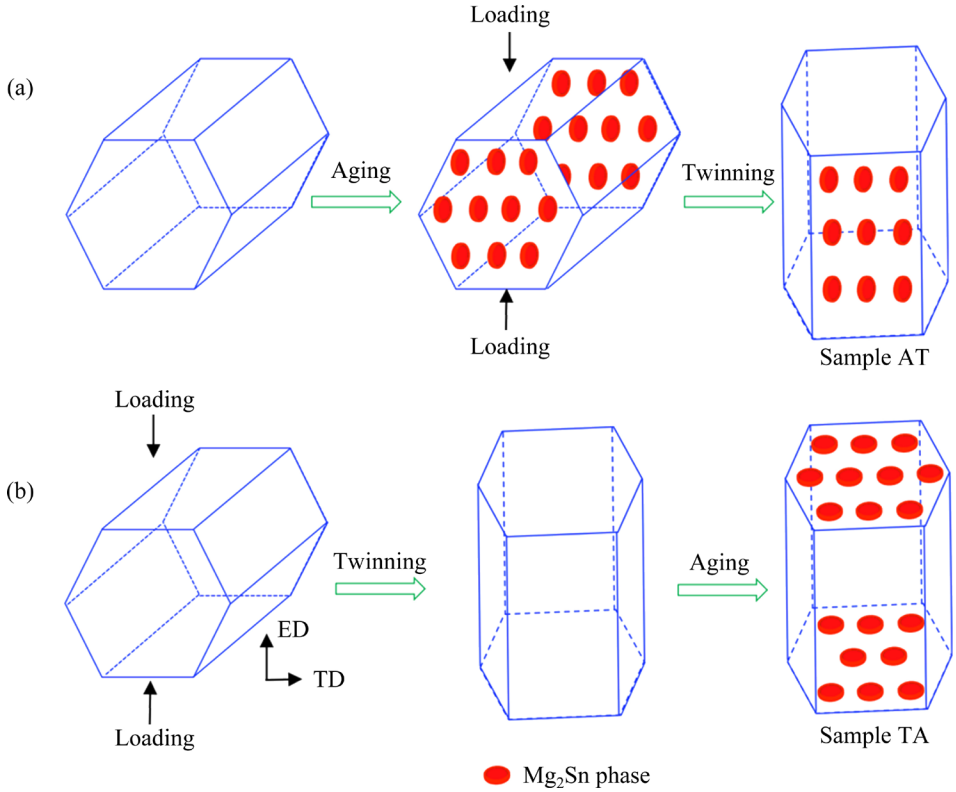

Fig. 1 Schematic diagrams of AT (a), TA (b) processes and samples produced in each step

obtained by the Archimedes method. The specific heat capacities of the samples in this study were obtained by the Neumann−Kopp rule [16,17]. Thermal conductivity (λ) was calculated from specific heat capacity (c_p), thermal diffusivity (α) and density (ρ) according to the following equation:

$$\lambda=\alpha\rho c_p$$

The thermal conductivity of each sample was tested three times, with the average value taken as the final result.

3 Results

3.1 EBSD observation

Figure 2 illustrates the EBSD maps and the corresponding (0002) pole figures of four different samples, showing the grain structure and orientation evolution of as-annealed sample, Samples A, TA and AT. The as-annealed sample exhibits a bimodal grain structure, and the average grain size of fine and coarse grains is (18.9±4.6) and (62.6±13.7) μm, respectively (Fig. 2(a)). And a typical $\langle 10\bar{1}0\rangle$ – $\langle 11\bar{2}0\rangle$ fiber texture with a maximum pole intensity of 8.24 m.r.d is presented in the as-annealed alloy, similar to other as-extruded Mg alloys [18,19]. In addition, Sample A presents a similar microstructure to as-annealed alloy, suggesting that grain structure and orientation are not changed after aging. Moreover, Samples TA and AT show a strong basal texture with the basal plane of most grains perpendicular to ED. Clearly, the compressive stress along ED, which is approximately perpendicular to the *c*-axis of grain, promotes the formation of the $\langle 0001\rangle$//ED texture component due to the occurrence of $\{10\bar{1}2\}$ tension twin reorienting the *c*-axis of the grains by 86.3° around $\langle 11\bar{2}0\rangle$ axis. The corresponding boundary misorientation angle distribution maps in Figs. 2(e) and (f) display three dominant peaks for low-angle grain boundaries (LAGBs), as well as high-angle grain boundaries (HAGBs) close to 60° and 86°. The peak at 86° sharing a strong $\langle \bar{1}2\bar{1}0\rangle$ rotation axis corresponds to $\{10\bar{1}2\}$ tension twin, suggesting that all the twins in Samples TA and AT are identified to be $\{10\bar{1}2\}$ tension twins. And the peak at about 60° $\langle 01\bar{1}0\rangle$ rotation axis is attributed to existence of $\{10\bar{1}2\}$ tension twin variants [20−22].

Furthermore, it is evident from Figs. 2(c) and (d) that the volume fraction of $\{10\bar{1}2\}$ tension twin in Sample TA (~91%) is higher than that of Sample AT (~79%) after being compressed to a

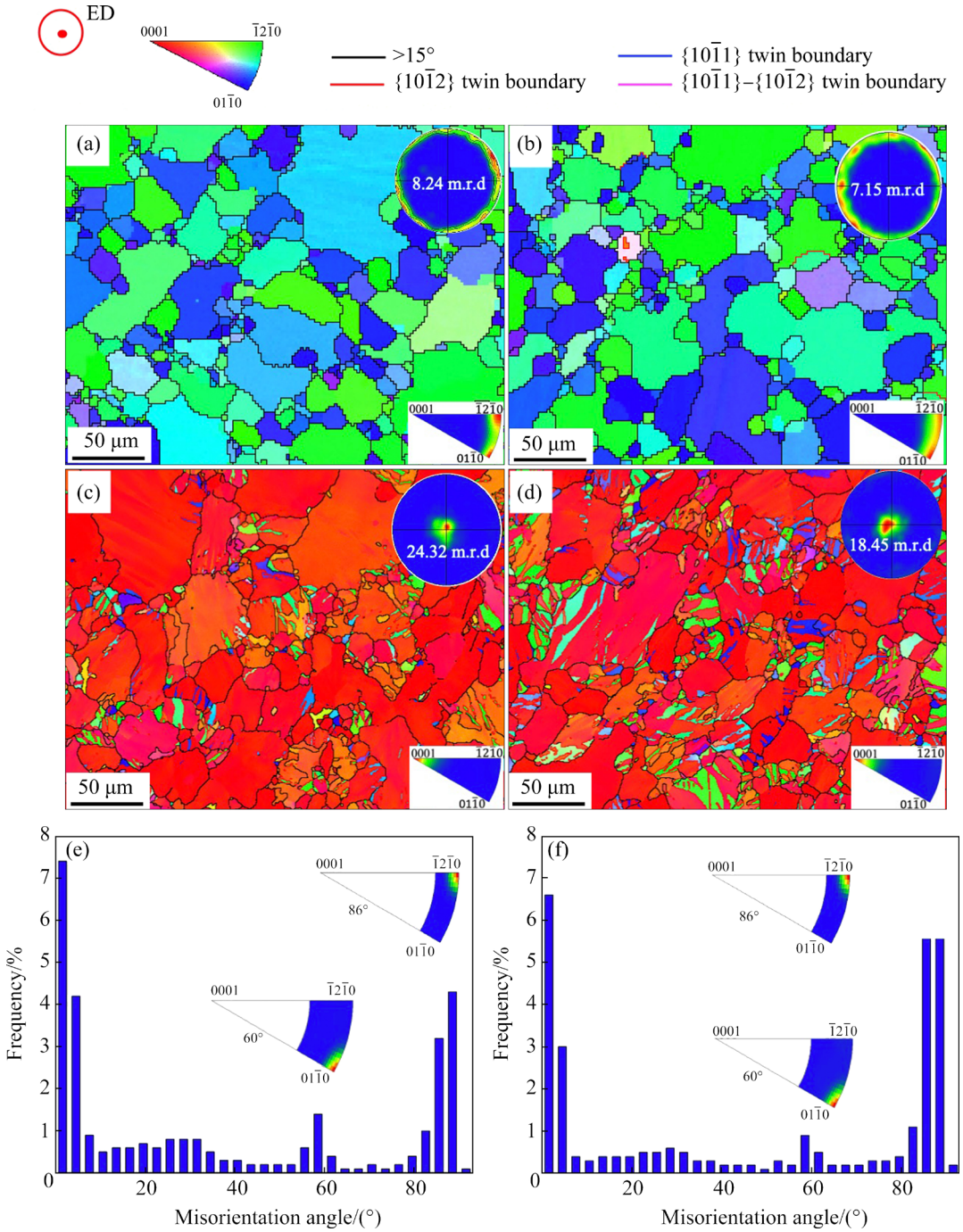

Fig. 2 EBSD maps and corresponding misorientation angle distribution maps: (a) As-annealed sample; (b) Sample A; (c, e) Sample TA; (d, f) Sample AT (The corresponding (0002) pole figures, texture intensities and misorientation angle with axis distribution for (60°±5°) and (86°±5°) are presented in the insets)

strain of 8% along ED. It is reasonable that the growth of tension twins in Sample AT is restricted due to the presence of a large number of precipitates during aging prior to twinning. Thus, the reorientation of basal Mg_2Sn precipitates and the resulting interactions between Mg_2Sn precipitates and twin boundary can be expected in Sample AT, and will be revealed and discussed in the next section.

3.2 Morphology and distribution of Mg_2Sn precipitates in Samples A, TA and AT

Figure 3 presents the TEM images of Samples A, TA and AT viewed along $[11\bar{2}0]$ and [0001], respectively. Some lath-shaped and polygon-shaped precipitates coexist in Sample A (Fig. 3(a)). And the long axis of lath-shaped precipitates is parallel to one certain direction as well as $(0001)_\alpha$ viewed along $[11\bar{2}0]_\alpha$, which is consistent with commonly

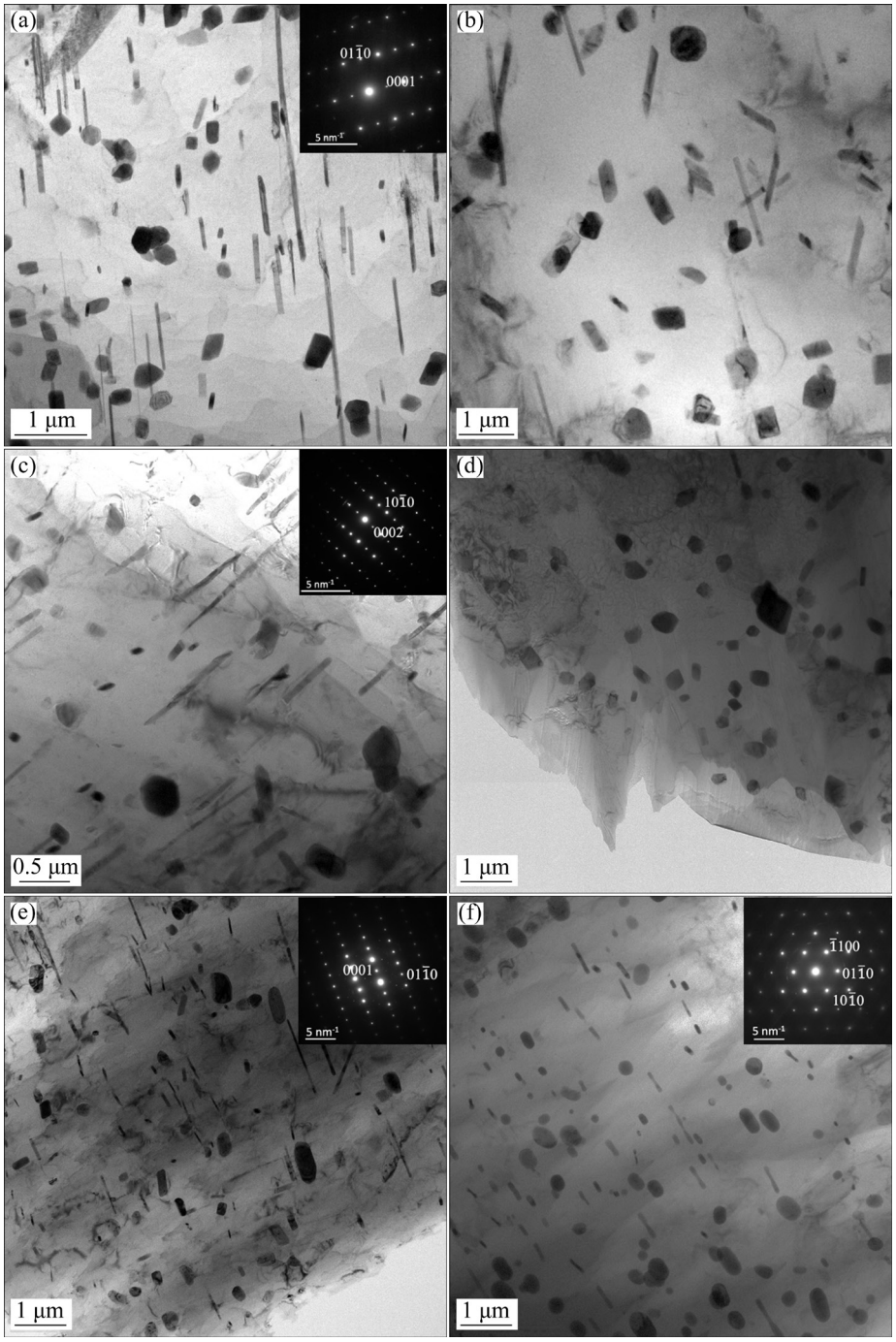

Fig. 3 Bright field TEM images of samples viewed along $[11\bar{2}0]$ (a, c, e) and [0001] (b, d, f): (a, b) Sample A; (c, d) Sample TA; (e, f) Sample AT

observed morphology characteristics in previous research [23,24]. Figure 3(b) also gives a bright field TEM image of Sample A viewed along $[0001]_\alpha$. The precipitates exhibit a random and uniform distribution without obvious directionality. Sample TA shows very similar features to Sample A including the morphology and distribution of precipitates viewed along $[11\bar{2}0]_T$ and $[0001]_T$, where the twin is labelled T, as demonstrated by TEM images shown in Figs. 3(c) and (d). For Sample AT, the long axis of lath-shaped precipitates viewed along $[11\bar{2}0]_T$ and $[0001]_T$ directions is nearly parallel to $(01\bar{1}0)_T$ rather than $(0001)_T$ shown in Figs. 3(e) and (f), which exhibits distinctly different distribution characteristics of precipitates compared with Samples A and TA. By comparing

the morphologies and distributions of precipitates in Samples A and TA with those of Sample AT, it is reasonable that AT treatment can alter the ORs between Mg_2Sn precipitates and α-Mg matrix, and precipitates lie on the prismatic plane instead of the basal plane of the α-Mg matrix, which agrees well with the predicted results in Fig. 1(b).

3.3 ORs between Mg_2Sn and α-Mg matrix in Sample TA

In Mg−Sn alloys, the primary strengthening phase is lath-shaped β-Mg_2Sn, which is commonly observed on the basal plane of α-Mg matrix. And the lattice parameters of a-Mg with an HCP structure are a=0.321 nm, c=0.521 nm, and that of β-Mg_2Sn, a face-centered cubic (FCC) structure, is $a=b=c$=0.6765 nm. Due to aging after twinning for Sample TA, β-Mg_2Sn particles still precipitate on the basal plane of the α-Mg matrix, so the ORs between precipitates and matrix are not changed compared to Sample A, which can be confirmed by Figs. 2(a−d) [25,26]. To determine the precise ORs between β-Mg_2Sn precipitates and α-Mg matrix, the TEM images and corresponding SAED patterns of Sample TA are given in Fig. 4. Figure 4(a) shows that precipitate has a wide range of morphologies, such as lath and polygon. The corresponding diffraction pattern of lath-shaped precipitate, and the simulated diffraction pattern by a PTCLab software are given in Figs. 4(b) and (c), respectively. According to the above results, the OR between this lath-shaped precipitate and α-Mg matrix can be expressed as: $[001]_\beta // [11\bar{2}0]_T$, $[1\bar{1}0]_\beta // [\bar{1}100]_T$, and $(110)_\beta // (0001)_T$ (OR1), which is consistent with previous results reported by CHEN et al [23,27]. As can be seen from Fig. 4(a), the long axis of lath-shaped precipitates is strictly parallel to the $(0002)_T$ plane. Furthermore, Fig. 4(d) shows the morphological characteristics of precipitates viewed along $[0001]_T$ direction. The SAED patterns of lath-shaped and polygon-shaped precipitates presented in Figs. 4(e) and (f) reveal that the OR between lath-shaped or polygon-shaped precipitates is: $[110]_\beta // [0001]_T$, $(1\bar{1}1)_\beta // (11\bar{2}0)_T$ and $(\bar{1}12)_\beta // (1\bar{1}00)_T$ (OR2). The above results validate that the multiple ORs between precipitates and α-Mg matrix in Sample TA are consistent with previous reports by CHEN et al [23,27].

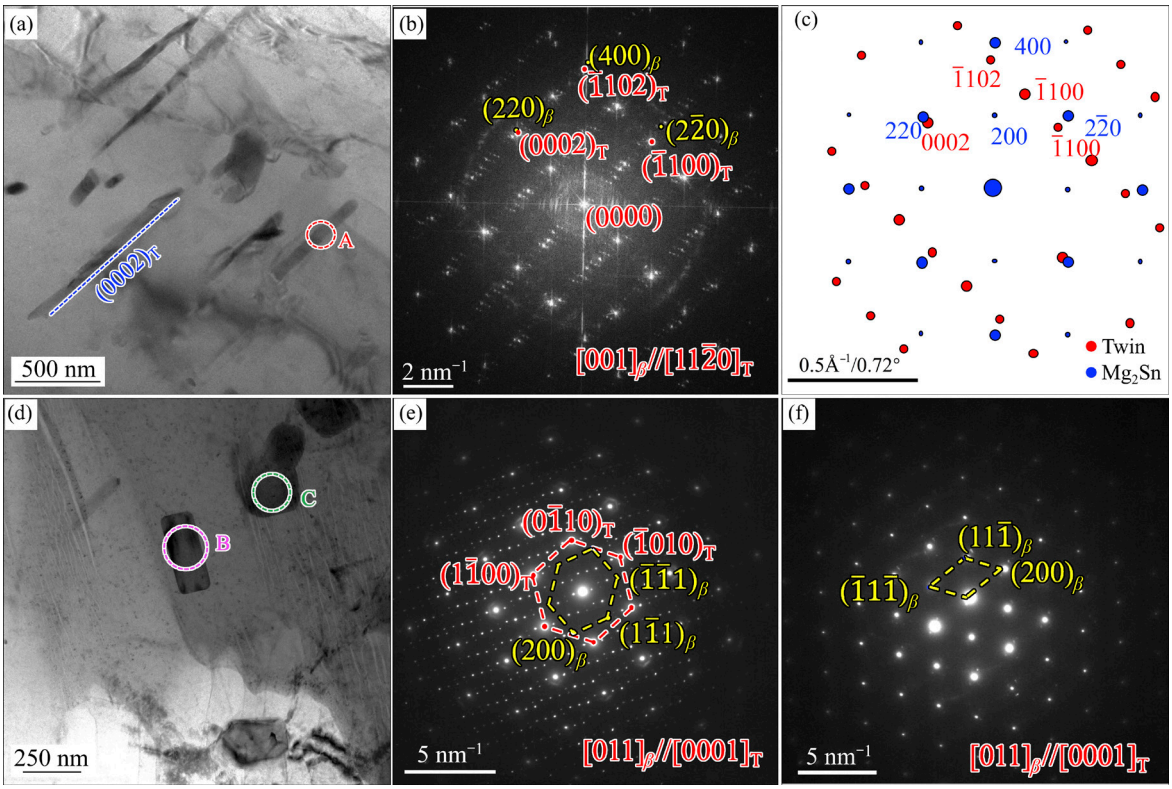

Fig. 4 Bright field TEM images of Sample TA viewed along $[11\bar{2}0]_T$ (a) and $[0001]_T$ (d), SAED pattern taken from Area *A* (b), corresponding simulated diffraction pattern of Area *A* (c), and SAED patterns taken from Areas *B* (e) and *C* (f)

3.4 ORs between Mg_2Sn and twin in Sample AT

According to previous research, aging prior to twinning treatment can alter the ORs between precipitates and α-Mg matrix [9,10,28]. The c-axis of grains can be reoriented by 86.3° around $\langle 11\bar{2}0\rangle$ axis due to the activation of $\{10\bar{1}2\}$ tension twin. At the same time, the precipitates would only experience a rigid body rotation in response to the twinning shear [12]. Therefore, to investigate the interaction between precipitates and twins, Sample A compressed to a strain of 2% is examined by TEM. Figure 5(a) shows that compressive stress along ED leads to the formation of a lenticular $\{10\bar{1}2\}$ tension twin inside the grain, which can be confirmed by SAED pattern of Area *B* in Fig. 5(b) (see Fig. 5(c)), and some lath-shaped precipitates locate at the twin boundary. To better reveal the microstructural details, a representative high-resolution TEM (HRTEM) micrograph taken from Area *C* in Fig. 5(b) is shown in Fig. 6(a). Based on the corresponding FFT pattern and simulated pattern by PTCLab shown in Figs. 6(b) and (c), the OR between precipitate and matrix can be expressed as: $[001]_\beta//[11\bar{2}0]_\alpha$, $(110)_\beta//(0001)_\alpha$, and $(1\bar{1}0)_\beta//(\bar{1}100)_\alpha$ (OR1). In contrast, the OR between the lath-shaped precipitate and the twin is: $[001]_\beta//[11\bar{2}0]_T$, $(110)_\beta$ ~3.7° from $(\bar{1}100)_T$, and $(1\bar{1}0)_\beta$ ~3.7° from $(0001)_T$ ($OR1_I^E$), where E stands for "experimental". The $(110)_\beta$ plane of precipitate is precisely parallel to the $(0002)_\alpha$ plane in the matrix but nearly parallel to the $(\bar{1}100)_T$ plane in the twin with a 3.7° deviation. The habit plane of lath-shaped precipitate at the twin boundary is nearly parallel to $(10\bar{1}0)_T$ plane rather than $(0001)_\alpha$ plane after twinning. The lath-shaped precipitate shown in Fig. 6(a) at twin boundary, which has not been swept by $\{10\bar{1}2\}$ twin boundary, has not experienced a rigid body rotation. This is consistent with a situation where the $\{10\bar{1}2\}$ tension twin has reoriented the matrix about 86.3° around the $\langle 11\bar{2}0\rangle$ axis rather than the precipitate; so that the angle between $(110)_\beta$ in the precipitate and $(10\bar{1}0)_T$ in the twin is about 3.7° [14]. Therefore, the OR between precipitates at the twin boundary and twin may be different from that between the precipitates embedded in the twin.

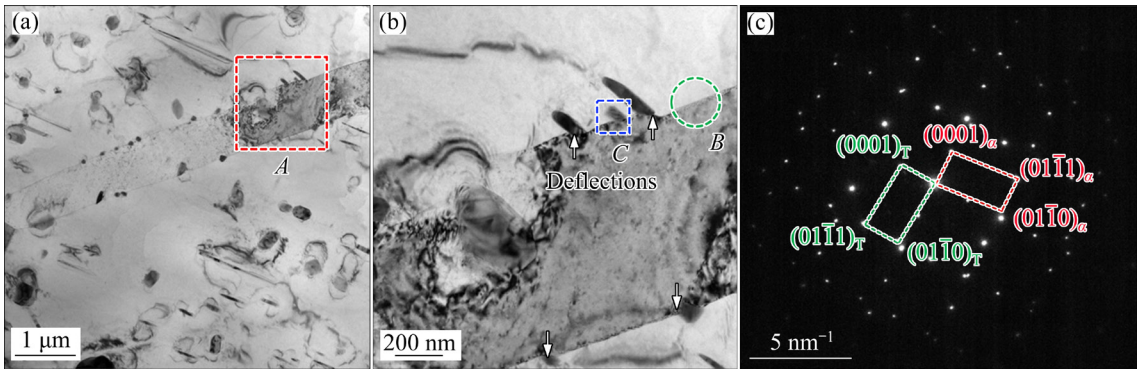

Fig. 5 Bright field TEM image of Sample A compressed to 2% strain along ED (a), high magnification TEM image of Area *A* (b), and SAED pattern of Area *B* (c) (The zone axis is $[11\bar{2}0]_\alpha$ direction of the matrix)

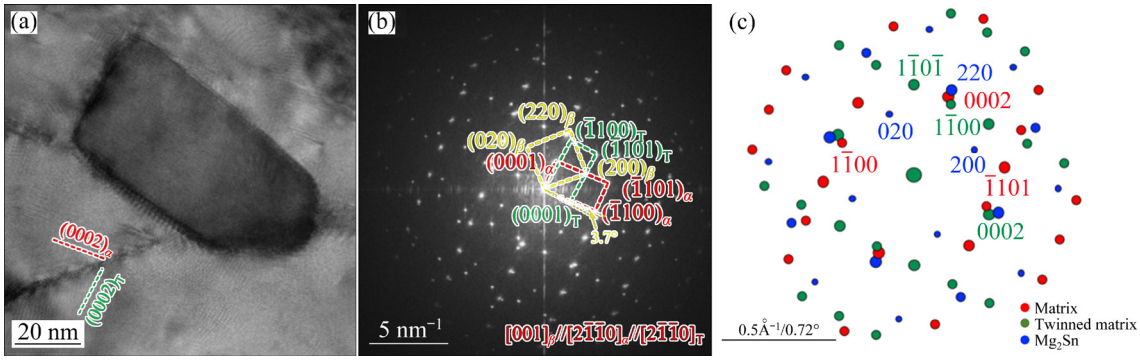

Fig. 6 Representative high-resolution TEM micrograph taken from Area *C* in Fig. 5(b) (a), FFT pattern (b), and corresponding simulated diffraction pattern (c) (The zone axis is $[11\bar{2}0]$ direction of the matrix and twin)

Figure 7(a) presents the TEM image of twin boundary crossing lath-shaped precipitates and some plate-shaped precipitates exist in the matrix and twin. The SAED pattern taken from Area *A* in Fig. 7(a) confirms that the twin boundary belongs to the $\{10\bar{1}2\}$ tension twin boundary (see Fig. 7(b)). The lath-shaped precipitates partially embedded in the twin, which have been partially swept by twin boundary, exhibit a rigid rotation of 3.7° to accommodate the twinning shear. As can be seen from Fig. 7(a), the long axis of lath-shaped precipitates located in the matrix is parallel to the $(0002)_\alpha$ of the matrix, which is strictly parallel to $(10\bar{1}0)_T$ in the twin.

To better understand the ORs between precipitates and twin, the TEM images, HRTEM images and corresponding SAED patterns of Sample AT in which precipitates are completely embedded in the $\{10\bar{1}2\}$ tension twin are given in Figs. 8 and 9. The TEM images of both lath-shaped precipitates in Sample AT are presented in Figs. 8(a) and (d), respectively. The corresponding SAED

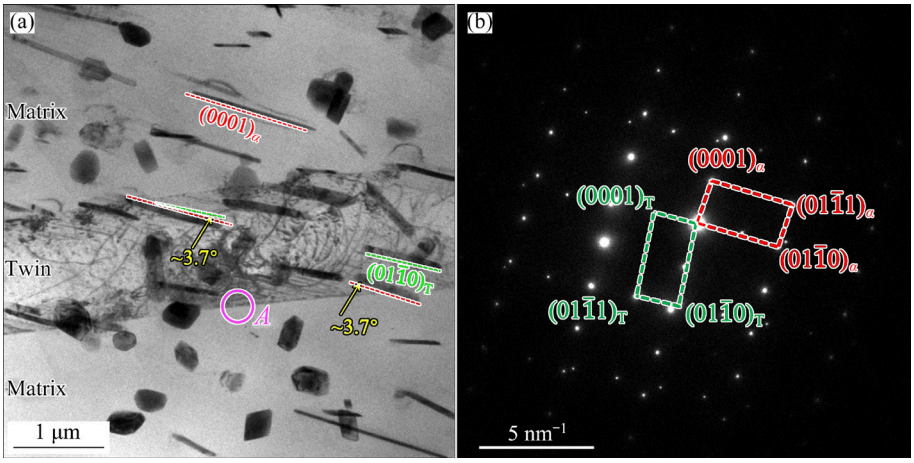

Fig. 7 Bight field TEM image of twin boundary crossing lath-shaped precipitates (a) and SAED pattern taken from Area *A* (b) (The zone axis is $[11\bar{2}0]$ direction of matrix and twin)

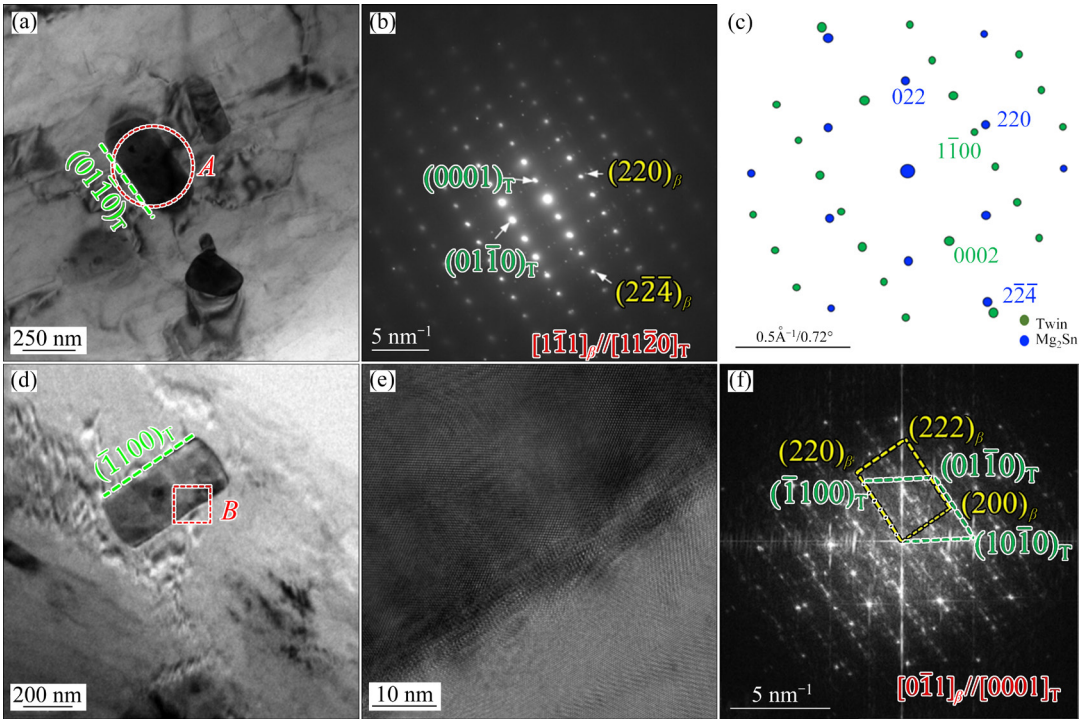

Fig. 8 TEM image (a), SAED pattern (b) and corresponding simulated diffraction pattern (c) of Area *A* viewed along $[11\bar{2}0]_T$ in Sample AT; (d) Bight field TEM image of lath-shaped precipitate in Area *B* viewed along $[0001]_T$ in Sample AT; (e) HRTEM micrograph taken from Area *B* in (d); (f) Corresponding FFT pattern of Area *B* in (d)

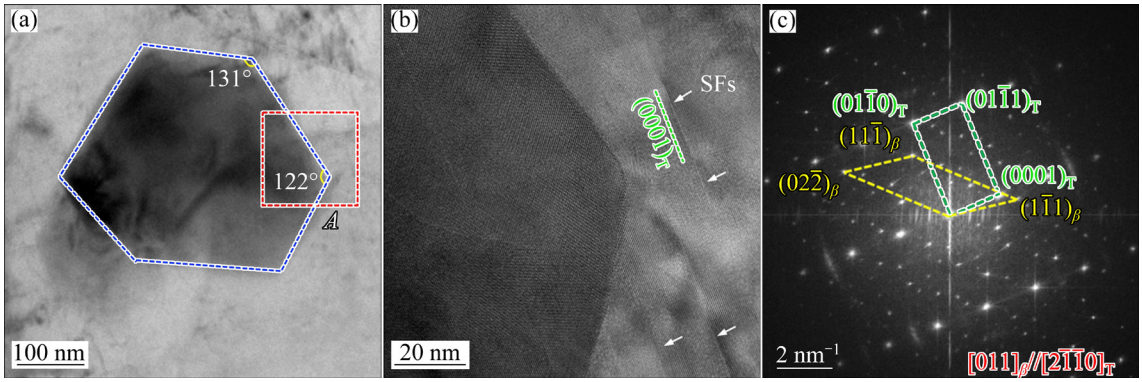

Fig. 9 Bright field TEM image of hexagon-shaped precipitate (a), HRTEM micrograph (b) taken from Area *A* in (a) and corresponding FFT pattern (c) of Area *A* in (a) (The zone axis is $[11\bar{2}0]_T$ direction of the twin)

pattern and simulated pattern of Area *A* given in Figs. 8(b) and (c) reveal that the OR between this lath-shaped precipitate and the twin is: $[1\bar{1}\,\bar{2}]_\beta//[0001]_T$, $(1\bar{1}\,1)_\beta//(11\bar{2}0)_T$, $(110)_\beta//(\bar{1}100)_T$ ($OR2^E$). The long axis of this lath-shaped precipitate is strictly parallel to $(10\bar{1}0)_T$ prismatic plane rather than $(0001)_T$ basal plane in the twin, which agrees well with the results shown in Fig. 7(a). The lath-shaped precipitate undergoes a rigid body rotation of 3.7° in response to the twinning shear. At the same time, the bright field image of lath-shaped Mg_2Sn precipitates viewed along $[0001]_T$ in Sample AT is shown in Fig. 8(d). Based on the corresponding HRTEM image and FFT pattern of Area *B* given in Figs. 8(e) and (f), it is revealed that the OR between this lath-shaped precipitate and the twin is: $[001]_\beta//[11\bar{2}0]_T$, $(110)_\beta//(\bar{1}100)_T$, and $(0\bar{1}1)_\beta//(0001)_T$ ($OR1_2^E$). Compared with OR1, it is revealed that the $(011)_\beta$ plane of the precipitate is strictly parallel to the $(10\bar{1}0)_T$ plane in the twin rather than $(0001)_T$ plane. The ORs for both lath-shaped precipitates given in Figs. 8(a) and (d) are consistent with results based on the crystallography-based algorithm proposed by LIU et al [28]. It is validated that the ORs between both lath-shaped precipitates can be regulated, and precipitates lie on the prismatic plane of the twin instead of basal plane of *α*-Mg matrix.

Both the lath-shaped precipitates given in Fig. 8 undergo a rigid rotation of 3.7° to accommodate twinning shear whether a rigid rotation of 3.7° is applicable to other types of precipitates. A TEM image of hexagon-shaped precipitate embedded in the twin in Sample AT viewed along $[2\bar{1}\bar{1}0]_T$ is presented in Fig. 9(a). The morphology of this hexagon-shaped precipitate is similar to previously reported precipitate with OR12: $[011]_\beta//[2\bar{1}\bar{1}0]_\alpha$, $[11\bar{1}]_\beta$ about 13.7° from $[0001]_\alpha$ [23,27]. The corresponding HRTEM of Area *A* shown in Fig. 9(b) reveals that a number of stacking faults (SFs) are also visible close to the precipitate in the twin. In addition, the corresponding FFT pattern given in Fig. 9(c) confirms that the OR between this hexagon-shaped precipitate and the twin is different from OR12 and can be expressed as: $[011]_\beta//[2\bar{1}\bar{1}0]_T$, $[11\bar{1}]_\beta$ about 10.2° from $[01\bar{1}0]_T$ ($OR12^E$). The activation of $\{10\bar{1}2\}$ tension twin rotates the matrix about 86.3° around $\langle 2\bar{1}\bar{1}0\rangle$ axis. The OR between precipitate and matrix has a rotation of 86.5° around $\langle 2\bar{1}\bar{1}0\rangle$ axis instead of 90°, which means that this hexagon-shaped precipitate undergoes a rigid rotation of 0.2° rather than 3.7°.

3.5 Thermal conductivity of Samples A, TA and AT

The thermal conductivity for samples under various conditions is given in Fig. 10. The thermal conductivity for as-annealed and pre-deformed alloys is 74.78 and 88.22 W/(m·K), respectively. In addition, the thermal conductivity of Samples A, TA and AT increases gradually with the increase of aging time. After aging for 500 h, thermal conductivity for Samples A, TA and AT increases to 105.34, 137.81 and 118.07 W/(m·K), respectively. Compared to as-annealed alloy, the thermal conductivity of pre-deformed alloy is increased by 13.44 W/(m·K), which is ascribed to the formation of $\{10\bar{1}2\}$ tension twin, leading to the *c*-axis of grains parallel to ED [29]. For Sample A, thermal conductivity increases by 30.56 W/(m·K) after aging for 500 h. Compared with pre-deformed alloy, the incremental thermal conductivity of Sample AT

is 29.85 W/(m·K), which is comparable to that of Sample A after aging for 500 h. In addition, thermal conductivity of Samples A and AT exhibits almost the same variation trend, as shown in Fig. 10. In comparison with pre-deformed alloy, the increment for thermal conductivity of Sample TA is 49.59 W/(m·K), which is much greater than that for Sample AT. This result indicates that the orientation of precipitates has a significant effect on the thermal conductivity of Mg alloys. And the lath-shaped Mg_2Sn precipitates lying on the (0001) basal plane perpendicular to ED are more beneficial to the improvement of thermal conductivity of the Mg−5Sn alloy than the lath-shaped Mg_2Sn precipitates lying on the $(10\bar{1}0)$ prismatic plane parallel to ED.

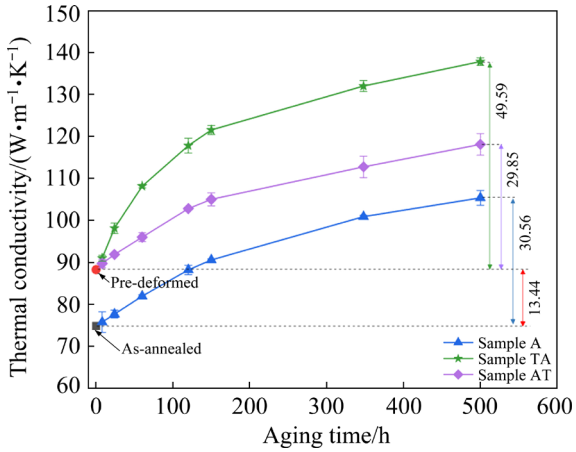

Fig. 10 Thermal conductivity variation of Samples A, TA and AT with aging time

4 Discussion

4.1 Evolution of ORs between precipitates and twin

As can be seen from Figs. 2(c) and (d), the volume fraction of $\{10\bar{1}2\}$ tension twin in Sample AT is lower than that in Sample TA. Figure 5(b) gives a common observation, showing that a twin boundary is deflected when particles are partially embedded in the twin boundary. It indicates that the precipitates partially embedded in the twin boundary will exert a strong pinning or drag effect on the twin boundary migration or propagation [13]. For Sample TA, the pre-compressive deformation is applied after annealing before aging treatment, which means almost no particles in the alloy. Concerning Sample AT, as can be seen from Figs. 5(a) and (b), the growth and coalescence of $\{10\bar{1}2\}$ tension twin are hindered by the precipitation of particles during aging prior to twinning treatments. The particles at the twin boundary will exert a pinning or drag effect on the boundary migration [30]. Therefore, the volume fraction of $\{10\bar{1}2\}$ tension twins in Sample AT is lower than that in Sample TA shown in Figs. 2(c) and (d).

With respect to Sample AT, however, the ORs between precipitates and twins have been regulated after twinning. For the lath-shaped precipitates presented in Figs. 8(a) and (d), according to $OR2^E$ and $OR1_2^E$, the OR between precipitates and matrix has a rotation of 90° around $\langle 2\bar{1}\bar{1}0\rangle$ axis, meaning that the lath-shaped precipitates precisely lie on the prismatic plane rather than basal plane. The activation of $\{10\bar{1}2\}$ tension twin rotates the matrix about 86.3° around $\langle 11\bar{2}0\rangle$ axis. In addition, the interactions between precipitates and twins need to be considered. The observations of relatively flat twin boundaries around the partially embedded lath-shaped precipitates shown in Fig. 7(a) suggest that twinning shear is a dominant mechanism for twin boundary migration [31]. In order to accommodate the twinning shear, these lath-shaped precipitates embedded in the twin undergo a rigid rotation of 3.7° around $\langle 11\bar{2}0\rangle$ axis. So, for lath-shaped precipitate with $OR2^E$, as shown in Fig. 8(b), it is clearly seen that the $(110)_\beta$ plane is exactly parallel to the $(10\bar{1}0)_T$ plane. And the $OR2^E$ can be expressed as: $[1\bar{1}2]_\beta // [0001]_T$, $(1\bar{1}1)_\beta // (11\bar{2}0)_T$, $(110)_\beta // (\bar{1}100)_T$. For lath-shape precipitate with $OR1_2^E$ shown in Fig. 8(f), the $(110)_\beta$ plane is exactly parallel to the $(\bar{1}100)_T$ plane, and the $OR1_2^E$ can be expressed as: $[001]_\beta // [11\bar{2}0]_T$, $(110)_\beta // (\bar{1}100)_T$, and $(0\bar{1}1)_\beta // (0001)_T$.

For hexagon-shaped precipitate shown in Fig. 9(a), according to $OR12^E$, the OR of precipitate has a rotation of 86.5° around $\langle 11\bar{2}0\rangle$ axis instead of 90°. After $\{10\bar{1}2\}$ tension twin, the matrix is rotated by 86.3° around $\langle 11\bar{2}0\rangle$ axis. There is a 3.5° deviation between the twin and the precipitate, which means that this precipitate only undergoes a rotation of 0.2° around $\langle 11\bar{2}0\rangle$ axis during the twinning. According to previous research, the nature of the interaction between the precipitates and the twins depends on the particle characteristics, such as precipitate thickness and shape [13,14,32−34]. The thickness of precipitate plays a crucial role in twin propagation and growth.

The angle of rotation is around 0.2°, which is far less than 3.7°. It confirms that the precipitate is not sheared but undergoes a rigid rotation in the twin to accommodate part of the twinning shear [13]. And the rotation angle of the precipitate caused by the twinning shear may vary slightly with a large thickness [32]. As can be seen from Fig. 9(a), the thickness for this hexagon-shaped precipitate is approximately 400 nm, which is much larger than that of lath-shaped precipitates with a thickness of about 200 nm. The strain around particles is very large without plastic accommodation at the particle/twin interface. Besides, as can be seen from Fig. 9(b), a number of SFs can be observed closely aligned with the precipitates in the twin. The existence of SFs may help to accommodate the strain at the particle/twin interface [33]. LIU et al [28] also found a similar pattern in Mg−Al alloy after twinning. The misalignment of atoms in SFs relieves part of the strain around the precipitates. Therefore, there is only a very small rotation of this hexagon-shaped precipitate embedded in the twin. The OR between this hexagon-shaped precipitate and the twin is: $[011]_{\beta}$// $[2\bar{1}\bar{1}0]_{\mathrm{T}}$, $[11\bar{1}]_{\beta}$ about 10.2° from $[01\bar{1}0]_{\mathrm{T}}$.

4.2 Effect of orientation of precipitates on thermal conductivity

As shown in Fig. 10, the thermal conductivity of samples in different states increases gradually with increasing the aging time. This is mainly attributed to the fact that the precipitation for the second phase can significantly decrease the content of heterogeneous solute atoms existing in the matrix after aging treatment. According to previous research, the thermal conductivity decrement caused by solute atoms matrix was about one order of magnitude larger than the second phase [35].

Furthermore, thermal conductivity of pre-deformed alloy is 13.44 W/(m·K) higher than that of as-annealed alloy. For as-annealed alloy, the *c*-axis is approximately perpendicular to ED. After pre-deformation, the occurrence of $\{10\bar{1}2\}$ tension twin rotates the *c*-axis of the grains by 86.3° around $\langle 11\bar{2}0\rangle$ axis to promote the formation of the *c*-axis// ED texture component. When the measurement direction is parallel to the ED, the direction of electrons and phonons is nearly parallel to the c-axis for pre-deformed alloy. The electrons and phonons scattered by defects in this direction become lower [29]. So, thermal conductivity can be improved after pre-deformation. The increment of thermal conductivity of Sample A-500 h to as-annealed alloy is 30.56 W/(m·K), which is higher than that of Sample AT-500 h to pre-deformed alloy (29.85 W/(m·K)). With the increase of aging time, the volume fraction of second phases increases gradually, which will exert a strong pinning or drag effect on the twin boundary migration or propagation. Thus, the volume fraction of $\{10\bar{1}2\}$ tension twin in Sample AT-500 h is smaller than that of pre-deformed alloy, as shown in Fig. 2. Therefore, the increment of thermal conductivity of Sample AT-500 h compared to pre-deformed alloy is smaller than that of Sample A-500 h compared to as-annealed alloy.

In addition, the increment of thermal conductivity for Sample TA compared to pre-deformed alloy is 49.59 W/(m·K), which is much greater than that for Sample AT. For Sample TA, the aging treatment is carried out after twinning, meaning that the β-Mg_2Sn particles still precipitate on the basal plane of the α-Mg matrix. The basal plane of α-Mg matrix is perpendicular to ED, and ED is parallel to the heat flow direction. So, the precipitates in Sample TA are perpendicular to the incident direction of heat flow. According to the above results, the precipitates in Sample AT are precisely transformed from basal precipitates to the prismatic precipitates. Therefore, the precipitates in Sample AT are parallel to the incident direction of heat flow. As can be seen from Fig. 10, the lath-shaped Mg_2Sn precipitates lying on the (0001) basal plane perpendicular to ED are more beneficial to the improvement of thermal conductivity of the Mg−5Sn alloy than the lath-shaped Mg_2Sn precipitates lying on the $(10\bar{1}0)$ prismatic plane parallel to ED. GAO et al [36] found a similar pattern that the precipitates parallel to the basal plane are more helpful to improve electromagnetic shielding than precipitates perpendicular to the basal plane when the measurement direction is perpendicular to the basal plane.

Due to the low diffusion rate of Sn atoms [37], the volume fraction of Mg_2Sn precipitates in Sample TA is comparable to that in Samples A and AT after aging at 200 ℃ for 500 h, which can be further confirmed by the TEM images shown in Fig. 3. This indicates that the difference in thermal conductivity between Samples TA and AT mainly

results from the different orientations of precipitates in two alloys. For Sample TA, the long axis of precipitates is perpendicular to the direction of heat flow; while the long axis of precipitates in Sample AT is parallel to the direction of heat flow. The heat conduction model of different orientation precipitates is presented in Fig. 11.

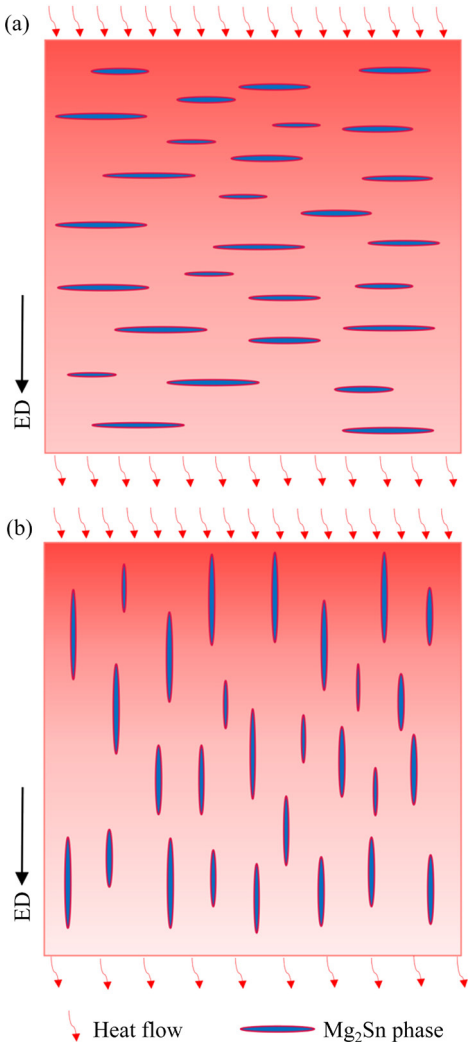

Fig. 11 Heat conduction model of different orientation precipitates: (a) Long axis of precipitates perpendicular to ED in Sample TA; (b) Long axis of precipitates parallel to ED in Sample AT

In general, thermal conductivity of precipitates is significantly lower than that of matrix [38]. Precipitates will act as scattering centers of electrons and phonons, and hinder the free movement of electrons and phonons. And then, the mean free path of electrons and phonons is decreased, and finally the thermal conductivity of alloys is reduced. The statistics shows that the thickness of most lath-shaped precipitates along the *c*-axis in Sample TA is less than 100 nm, which is smaller than the mean free path of electrons and phonons (~100 nm) [35], And the interspace between precipitates is larger than 100 nm. So, the lath-shaped precipitates in Sample TA have little effect on thermal conductivity of alloys; while the thickness of most lath-shaped precipitates along *c*-axis in Sample AT is in the range of 160−450 nm. According to previous research, the microstructure with a larger length of precipitates along the heat flow direction had a lower thermal conductivity. The larger the length of precipitates along the heat flow direction is, the more serious the scattering of electrons and phonons is, and the more the decrease in the mean free path of electrons and phonons is [39]. That is, the larger the size of precipitates parallel to the direction of movement of electrons and phonons is, the lower the thermal conductivity of the alloy is. Therefore, the thermal conductivity of Sample AT is lower than that of Sample TA, and the Sample TA shows the highest thermal conductivity of 137.81 W/(m·K), with the long axis of precipitates and the basal plane of grains perpendicular to ED.

The present experimental results indicate that controlling the orientation of precipitates in Mg alloys is an effective method for developing high strength and thermal conductivity synergy in Mg alloys.

5 Conclusions

(1) EBSD analysis reveals that the compressive stress along ED can promote the formation of $\{10\bar{1}2\}$ tension twin, which can reorient the *c*-axis of the grains by 86.3°. The presence of precipitates can exert a strong pinning or drag effect on the twin boundary migration or propagation. The volume fraction of $\{10\bar{1}2\}$ tension twin in Sample AT is lower than that in Sample TA.

(2) The lath-shaped precipitates in Sample AT experience a rigid rotation of 3.7° to accommodate the twinning shear. The precipitates in Mg−5Sn alloy are precisely transformed from basal precipitates to the prismatic precipitates. For hexagon-shaped precipitate with a large thickness in Sample AT, the stacking faults developed in the twin help to coordinate a part of strain at the particle/twin interface. There is only a small

rotation of this hexagon-shaped precipitate. The OR between this hexagon-shaped precipitate and twin can be expressed as: $[011]_{\beta}//[2\bar{1}\bar{1}0]_{T}$, $[11\bar{1}]_{\beta}$ about 10.2° from $[01\bar{1}0]_{T}$.

(3) The orientation of precipitates has a significant influence on the thermal conductivity of Mg alloys. The lath-shaped precipitates lying on the (0001) basal plane perpendicular to ED are more beneficial to the improvement of thermal conductivity of the Mg−5Sn alloy than the precipitates lying on the $(10\bar{1}0)$ prismatic plane parallel to ED. Sample TA shows the best thermal conductivity of 137.81 W/(m·K), with the long axis of precipitates and the basal plane of grains perpendicular to ED.

Acknowledgments

The authors are grateful for the financial supports from the National Natural Science Foundation of China (No. 51901144) and the Anhui Provincial Natural Science Foundation, China (No. 2108085QE185).

References

[1] WANG Chun-peng, XIN Ren-long, LI Dong-rong, SONG Bo, WU Ming-yu, LIU Qing. Enhancing the age-hardening response of rolled AZ80 alloy by pre-twinning deformation [J]. Materials Science and Engineering A, 2017, 680: 152−156.

[2] ZHANG Wan-peng, MA Ming-long, YUAN Jia-wei, SHI Guo-liang, LI Yong-jun, LI Xing-gang, ZHANG Kui. Microstructure and thermophysical properties of Mg−2Zn−*x*Cu alloys [J]. Transactions of Nonferrous Metals Society of China, 2020, 30(7): 1803−1815.

[3] LI Shu-bo, YANG Xin-yu, HOU Jiang-tao, DU Wen-bo. A review on thermal conductivity of magnesium and its alloys [J]. Journal of Magnesium and Alloys, 2020, 8(1): 78−90.

[4] BAZHENOV V E, KOLTYGIN A V, SUNG M C, PARK S H, TSELOVALNIK Y V, STEPASHKIN A A, RIZHSKY A A, BELOV M V, BELOV V D, MALYUTIN K V. Development of Mg–Zn–Y–Zr casting magnesium alloy with high thermal conductivity [J]. Journal of Magnesium and Alloys, 2021, 9(5): 1567−1577.

[5] ZHONG Li-ping, WANG Yong-jian, GONG Min, ZHENG Xing-wen, PENG Jian. Effects of precipitates and its interface on thermal conductivity of Mg−12Gd alloy during aging treatment [J]. Materials Characterization, 2018, 138: 284−288.

[6] WANG Chun-ming, CUI Zhi-ming, LIU Hong-mei, CHEN Yun-gui, DING Wu-cheng, XIAO Su-fen. Electrical and thermal conductivity in Mg–5Sn Alloy at different aging status [J]. Materials & Design, 2015, 84: 48−52.

[7] YU Da-liang, ZHANG Ding-fei, SUN Jing, LUO Yuan-xin, XU Jun-yao, ZHANG Hong-ju, PAN Fu-sheng. High cycle fatigue behavior of extruded and double-aged Mg−6Zn−1Mn alloy [J]. Materials Science and Engineering A, 2016, 662: 1−8.

[8] CHENG Wei-li, TIAN Liang, WANG Hong-xia, BIAN Li-ping, YU Hui. Improved tensile properties of an equal channel angular pressed (ECAPed) Mg−8Sn−6Zn−2Al alloy by prior aging treatment [J]. Materials Science and Engineering A, 2017, 687: 148−154.

[9] LIU Fei-ya, XIN Ren-long, WANG Chun-peng, SONG Bo, LIU Qing. Regulating precipitate orientation in Mg−Al alloys by coupling twinning, aging and detwinning processes [J]. Scripta Materialia, 2019, 158: 131−135.

[10] WAN Y J, ZENG Y, ZENG Q, SONG B, HUANG X F, QIAN X Y, JIANG B. Simultaneously improved strength and toughness of a Mg−Sn alloy through abundant prismatic lath-shaped precipitates [J]. Materials Science and Engineering A, 2021, 811: 141087.

[11] WAN Y J, ZENG Y, DOU Y C, HU D C, QIAN X Y, ZENG Q, SUN K X, QUAN G F. Improved mechanical properties and strengthening mechanism with the altered precipitate orientation in magnesium alloys [J]. Journal of Magnesium and Alloys, 2022, 10(5): 1256−1267.

[12] GENG J, CHUN Y B, STANFORD N, DAVIES C H J, NIE J F, BARNETT M R. Processing and properties of Mg−6Gd−1Zn−0.6Zr: Part 2. Mechanical properties and particle twin interactions [J]. Materials Science and Engineering A, 2011, 528(10): 3659−3665.

[13] ROBSON J D, STANFORD N, BARNETT M R. Effect of precipitate shape and habit on mechanical asymmetry in magnesium alloys [J]. Metallurgical and Materials Transactions A, 2013, 44(7): 2984−2995.

[14] GHARGHOURI A, WEATHERLY G C, D M J. The interaction of twins and precipitates in a Mg−7.7at.%Al alloy [J]. Philosophical Magazine A, 1998, 78(5): 1137−1149.

[15] GU X F, FURUHARA T, ZHANG W Z. PTCLab: Free and open-source software for calculating phase transformation crystallography [J]. Journal of Applied Crystallography, 2016, 49(3): 1099−1106.

[16] RUDAJEVOVÁ A, von BUCH F, MORDIKE B L. Thermal diffusivity and thermal conductivity of MgSc alloys [J]. Journal of Alloys and Compounds, 1999, 292(1/2): 27−30.

[17] RUDAJEVOVÁ A, LUKÁČ P. Comparison of the thermal properties of AM20 and AS21 magnesium alloys [J]. Materials Science and Engineering A, 2005, 397(1/2): 16−21.

[18] WANG Yong-jian, ZHONG Li-ping, DOU Yu-chen, ZHANG Xiao-feng. Revealing grain structure development and texture evolution during elastic stress-assist aging of Mg−Zn alloys [J]. Journal of Alloys and Compounds, 2021, 881: 160474.

[19] JIA Qing-gong, ZHANG Wen-xin, SUN Yi, XU Chun-xiang, ZHANG Jin-shan, KUAN Jun, Microstructure and mechanical properties of as-cast and extruded biomedical Mg−Zn−Y−Zr−Ca alloy at different temperatures [J]. Transactions of Nonferrous Metals Society of China, 2019, 29(3): 515−525.

[20] GUAN Di-kai, RAINFORTH W M, MA L, WYNNE B, GAO Jun-heng. Twin recrystallization mechanisms and exceptional contribution to texture evolution during annealing in a magnesium alloy [J]. Acta Materialia, 2017, 126: 132−144.

[21] JIANG M G, XU C, YAN H, FAN G H, NAKATA T, LAO C S, CHEN R S, KAMADO S, HAN E H, LU B H.

Unveiling the formation of basal texture variations based on twinning and dynamic recrystallization in AZ31 magnesium alloy during extrusion [J]. Acta Materialia, 2018, 157: 53−71.
[22] JIANG M G, YAN H, CHEN R S. Microstructure, texture and mechanical properties in an as-cast AZ61 Mg alloy during multi-directional impact forging and subsequent heat treatment [J]. Materials & Design, 2015, 87: 891−900.
[23] CHEN Hong-ting, SHI Zhang-zhi. A new orientation relationship OR13 and irrational interfaces between Mg_2Sn phase and magnesium matrix in an aged Mg alloy [J]. Materials Letters, 2020, 281: 128648.
[24] LIU C Q, CHEN H W, LIU H, ZHAO X J, NIE J F. Metastable precipitate phases in Mg−9.8wt.%Sn alloy [J]. Acta Materialia, 2018, 144: 590−600.
[25] ZHENG K Y, DONG J, ZENG X Q, DING W J. Effect of pre-deformation on aging characteristics and mechanical properties of a Mg−Gd−Nd−Zr alloy [J]. Materials Science and Engineering A, 2008, 491(1/2): 103−109.
[26] SHI Guo-liang, ZHANG Ding-fei, ZHANG Hong-ju, ZHAO Xia-bing, QI Fu-gang, ZHANG Kui. Influence of pre-deformation on age-hardening response and mechanical properties of extruded Mg−6%Zn−1%Mn alloy [J]. Transactions of Nonferrous Metals Society of China, 2013, 23(3): 586−592.
[27] SHI Zhang-zhi, CHEN Hong-ting, ZHANG Ke, DAI Fu-zhi, LIU Xue-feng. Crystallography of precipitates in Mg alloys [J]. Journal of Magnesium and Alloys, 2021, 9(2): 416−431.
[28] LIU F Y, XIN R L, ZHANG M X, PÉREZ-PRADO M T, LIU Q. Evaluating the orientation relationship of prismatic precipitates generated by detwinning in Mg alloys [J]. Acta Materialia, 2020, 195: 263−273.
[29] ZHONG Li-ping, WANG Yong-jian, LUO Hong, LUO Chang-sen, PENG Jian. Evolution of the microstructure, texture and thermal conductivity of as-extruded ZM60 magnesium alloy in pre-compression [J]. Journal of Alloys and Compounds, 2019, 775: 707−713.
[30] HE Jie-jun, LIU Tian-mo, XU Shun, ZHANG Yin. The effects of compressive pre-deformation on yield asymmetry in hot-extruded Mg−3Al−1Zn alloy [J]. Materials Science and Engineering A, 2013, 579: 1−8.
[31] XIE K Y, ZHAO D X, LEU B, MA X L, JIAO Q, EL-AWADY J A, WEIHS T P, BEYERLEIN I J, KUMAR M A. Understanding the interaction of extension twinning and basal-plate precipitates in Mg−9Al using precession electron diffraction [J]. Materialia, 2021, 15: 101044.
[32] SISKA F, STRATIL L, CIZEK J, GUO T T, BARNETT M. Numerical analysis of twin-precipitate interactions in magnesium alloys [J]. Acta Materialia, 2021, 202: 80−87.
[33] STANFORD N, BARNETT M R. Effect of particles on the formation of deformation twins in a magnesium-based alloy [J]. Materials Science and Engineering A, 2009, 516(1/2): 226−234.
[34] STANFORD N, GENG J, CHUN Y B, DAVIES C H J, NIE J F, BARNETT M R. Effect of plate-shaped particle distributions on the deformation behaviour of magnesium alloy AZ91 in tension and compression [J]. Acta Materialia, 2012, 60(1): 218−228.
[35] EIVANI A R, AHMED H, ZHOU J, DUSZCZYK J. Correlation between electrical resistivity, particle dissolution, precipitation of dispersoids, and recrystallization behavior of AA7020 aluminum alloy [J]. Metallurgical and Materials Transactions A, 2009, 40(10): 2435−2446.
[36] GAO S, CHEN X, PAN F, SONG K, ZHAO C, LIU L, LIU X, ZHAO D. Effect of secondary phase on the electromagnetic shielding effectiveness of magnesium alloy [J]. Scientific Reports, 2018, 8(1): 1−14.
[37] SASAKI T T, ELSAYED F R, NAKATA T, OHKUBO T, KAMADO S, HONO K. Strong and ductile heat-treatable Mg−Sn−Zn−Al wrought alloys [J]. Acta Materialia, 2015, 99: 176−186.
[38] SU C Y, LI J, LUO A A, YING T, ZENG X Q. Effect of solute atoms and second phases on the thermal conductivity of Mg−RE alloys: A quantitative study [J]. Journal of Alloys and Compounds, 2018, 747: 431−437.
[39] LEE W J, LEE J K, KYOUNG W M, LEE H, LEE H J, KIM D C. Effect of inhomogeneous composition on the thermal conductivity of an Al alloy during the precipitation-hardening process [J]. Journal of Materials Research and Technology, 2020, 9(5): 10139−10147.

Mg−5Sn 合金中析出相取向演变及其对合金热导率的影响

钟丽萍，王永建

安徽工业大学 冶金工程学院 微纳组织与力学研究所，马鞍山 243002

摘　要：系统研究 Mg−5Sn 合金在不同处理条件下析出相取向的演变及其对合金热导率的影响。结果表明，在先时效后孪生处理的合金(样品 AT)中，基面析出相被调整为柱面析出相，并且板条状析出相发生 3.7°的刚性转动以协调孪晶剪切；而样品 AT 中厚度较大的六边形析出相则只发生了 0.2°的刚性转动，这是由于堆垛层错能够释放部分析出相/孪晶界的应变。此外，析出相的取向显著影响合金的热导率。当热导率测试方向平行于挤压方向时，与平行于挤压方向的柱面析出相相比，垂直于挤压方向的基面析出相更有利于合金热导率的提高。基面有析出相的 TA(先孪生后时效处理)样品具有最佳的热导率(137.81 W/(m·K))。

关键词：析出相；位向关系；热导率；Mg−Sn 合金

(Edited by Wei-ping CHEN)